El-Bahay *et al.*
Protection and Control of Modern Power Systems (2023) 8:14
https://doi.org/10.1186/s41601-023-00289-8

Protection and Control of
Modern Power Systems

ORIGINAL RESEARCH **Open Access**

Effective participation of wind turbines in frequency control of a two-area power system using coot optimization

Mahmoud Hussain El-Bahay[1*], Mohammed Elsayed Lotfy[1] and Mohamed A. El-Hameed[1,2]

Abstract

In this paper, load frequency control is performed for a two-area power system incorporating a high penetration of renewable energy sources. A droop controller for a type 3 wind turbine is used to extract the stored kinetic energy from the rotating masses during sudden load disturbances. An auxiliary storage controller is applied to achieve effective frequency response. The coot optimization algorithm (COA) is applied to allocate the optimum parameters of the fractional-order proportional integral derivative (FOPID), droop and auxiliary storage controllers. The fitness function is represented by the summation of integral square deviations in tie line power, and Areas 1 and 2 frequency errors. The robustness of the COA is proven by comparing the results with benchmarked optimizers including: atomic orbital search, honey badger algorithm, water cycle algorithm and particle swarm optimization. Performance assessment is confirmed in the following four scenarios: (i) optimization while including PID controllers; (ii) optimization while including FOPID controllers; (iii) validation of COA results under various load disturbances; and (iv) validation of the proposed controllers under varying weather conditions.

Keywords Coot optimizer, FOPID, Load frequency control, Photovoltaic, Variable speed wind turbine

1 Introduction

Renewable energy sources (RES) are promising alternatives to fossil fuels due to the exhaustion of fossil fuels and their negative environmental effects [1]. The frequency of a power system deviates from its nominal value because of continuous load changes and other disturbances [2]. Stored kinetic energy (*KE*) in the rotors of conventional synchronous generators (SG) will tolerate normal load changes until the operation of primary and secondary frequency regulation loops [3]. Power systems with a high penetration of RES have less *KE* owing to the reduction of inherent inertia with the increase of RES [4]. Thus, problems in power system stability and frequency regulation may be initiated [3, 4]. In this paper, participation of RES and energy storage devices for frequency support is discussed for a two-area power system. Frequency support is performed by a new optimization algorithm, namely, the Coot Optimization Algorithm (COA). The COA is robust in allocating the optimal parameters of the fractional order proportional integral derivative (FOPID) controllers, washout filter controller and droop controller.

Energy storage systems play an essential role in the frequency regulation of a power system [5]. Battery energy storage (BES) is selected in [6, 7] to adjust the frequency of a microgrid integrated with wind turbines (WT) while superconducting magnetic energy storage (SMES) is proposed for frequency regulation in [8, 9]. In addition, supercapacitor energy storage (SCES) is proposed in [10,

*Correspondence:
Mahmoud Hussain El-Bahay
mahhussen@zu.edu.eg
[1] Electrical Power and Machines Department, Faculty of Engineering, Zagazig University, Zagazig 44519, Egypt
[2] ECEN Department, Faculty of Engineering, A'Sharqiyah University, 400 Ibra, Oman

11] to control the frequency of a microgrid integrated with PV and tidal energy.

One technique for RES participation in frequency support is de-loading, where some reserves of active power in RES is maintained to support sudden load increase. Overvoltage de-loading of PV is illustrated in [12, 13] to tolerate load disturbance while overspeed and pitch angle control of variable speed wind turbine (VSWT) are discussed in [14–16]. Another technique is inertial response, which momentarily supports a power system by additional active power extracted from a VSWT. Recently, extensive research has been done to enhance the inertia of a power system with high penetration of RES using virtual inertial response techniques. Inertial response is classified into fast power reserve, hidden inertia, and droop control. In [17, 18], fast power reserve is used to enhance power system inertia while hidden inertia is proposed in [19, 20]. A droop controller, which is proposed in this paper, is demonstrated for inertial response and effective frequency regulation in [21–23].

Power system stability during load disturbance is achieved by load frequency control (LFC) which is a secondary control loop used to eliminate errors in frequency and tie line power [24]. Proportional integral derivative (PID) controllers have been benchmarked in many LFC studies. In [25], the dynamic performance of an offshore grid-connected wind farm is enhanced by flywheel energy storage (FWES) based on a PID controller. In [8], LFC of a power system considering high penetration of wind power is illustrated by SMES based on a PID controller. In [26], LFC is performed by a PID droop controller for a two-area power system highly penetrated with wind power, whereas in [27], LFC is performed by an adaptive PID droop controller for an isolated power system also highly penetrated with wind power. Also, LFC is illustrated in [28] using a two-degrees-of-freedom PID for a three-area power system integrated with plug-in electric vehicles (EVs).

The fractional order PID (FOPID) controller is validated and its robustness proved to be better than a traditional PID because of the higher number of its tunable parameters [24]. In [29], LFC is examined for a two-area power system by two-degrees-of-freedom FOPID. In addition, in [30], LFC is equipped for a microgrid integrated with VSWT using droop control-based FOPID, whereas in [31], LFC is demonstrated using FOPID for a single area containing hydro, reheat and non-reheat turbines. A lot of studies have been devoted to illustrating the optimization algorithms which are used to.

tune power system parameters. In [21], LFC is reinforced using BES for PV and extracting the *KE* from VSWT by tuning the parameters of the PID controller using a stochastic fractal optimizer. In [32], optimal charging of EVs for LFC is performed by allocating the parameters of a PI controller using a genetic algorithm. Optimum parameters of the PID controller are obtained in [33] using firefly and particle swarm optimization (PSO) to achieve optimal LFC using hybrid FWES and BES, while optimal parameters of the PI controller are obtained in [34] by a sine cosine algorithm to optimize the LFC using SCES. In [35], LFC is performed by optimizing the parameters of the PID controllers of SMES and BES using a social spider optimizer. Parameters of an FOPID controller for optimal LFC are obtained in [24] and [36] by a modified hunger games search optimizer and chaotic multi-objective optimizer, respectively.

Frequency regulation of a two-area power system is performed in this paper by COA which allocates the parameters of the FOPID controller. COA is a novel algorithm and has been validated as a robust optimizer in many studies [37, 38]. In [39], COA is validated for optimal parameter extraction of a lithium-ion battery when compared to other six benchmarked optimizers. Optimal sizing of the energy storage system required to support a wind power producer is obtained in [40] by COA, which proves its robustness compared to two other benchmarked optimizers. The paper seeks a novel algorithm while performing LFC for the proposed two-area power system, and COA, HBA and AOS are chosen as the novel robust optimizers, while their fitness is compared with PSO and WCA which are well known and are used as the benchmarked optimizers. From the results, COA proves its robustness over HBA, AOS, PSO and WCA.

The proposed model is a two-area power system. Area 1 contains steam SG and has 50% penetration of wind power, while Area 2 contains hydro SG and has 20% penetration of solar power in addition to an auxiliary storage system. COA is validated first by comparing the optimization results while including PID controller as the benchmark, and robust optimizers such as atomic orbital search optimizer (AOS) [41], honey badger algorithm (HBA) [42], water cycle algorithm (WCA) and PSO. Then PID controllers are replaced by FOPID controllers and the optimization is performed again by the same five optimizers to validate the robustness of COA. COA results are benchmarked and validated for its robustness under variable load disturbances and varying weather conditions.

The main outcomes of this paper are:

(a) A novel application of COA is proposed for parameter extraction of FOPID frequency controllers.
(b) LFC are supported via droop controller for inertial response of WT, pitch angle supplementary controller, and transient support of stored energy.

(c) Benchmarking with challenging optimization methods is incorporated for the validation of the proposed method.
(d) Different scenarios are studied to investigate the robustness of the designed controllers.

The remainder of the paper is structured as follows. Modelling of the two-area power system is discussed in Sect. 2, and Sect. 3 illustrates the algorithm of COA. Simulation results for different scenarios are demonstrated in Sect. 4, and the outcomes of this paper are discussed in Sect. 5.

2 System modelling

The intended system is a two-area power system shown in Fig. 1. It consists of conventional plants and different RES such as type 3 wind turbines and PV systems. Area 1 consists of 50% conventional steam turbine and 50% VSWT. The output power of the conventional steam turbine is represented by P_{m1} while the output electrical power of the VSWT is represented by P_e in Fig. 1. Area 2 consists of 80% conventional hydro turbine and 20% solar energy, with the output power of the conventional hydro turbine represented by P_{m2} and the solar energy represented by P_{PV} in Fig. 1.

2.1 Model of type 3 wind turbine

A type 3 WT with a rating of 3.6 MW is proposed in this model. Its parameters are given in Table 1 [43]. The block diagram of the type 3 WT is illustrated in Figs. 2, 4 and 5 [43]. The PI controller in Fig. 2 gives an output torque signal depending on the WT speed deviation. This model is selected to estimate the dynamic operation of the intended two-area power system during any power disturbances. The output WT mechanical power is illustrated by:

$$P_m = 0.5 \times \rho \times A_{wt} \times {V_w}^3 \times C_p \tag{1}$$

where the air density is ρ (kg/m^3), the blade swept area is A_{wt} (m^2), the wind speed is V_w (assumed 11 m/s), and the coefficient of performance is C_p given as:

$$C_p = \sum_{k=0}^{4}\sum_{n=0}^{4} \alpha_{k,n}\lambda^n\beta^k \tag{2}$$

where β is the blade pitch angle and $\alpha_{k,n}$ are constants illustrated in [43]. λ is the WT tip speed ratio given as:

$$\lambda = \frac{K_b \times \omega_{wt}}{V_w} \tag{3}$$

where the rotor speed is denoted by ω_{wt} and the WT radius is represented by K_b. The relations between the output mechanical power of the WT and its speed at different wind speeds are demonstrated in Fig. 3. Maximum power point tracking (MPPT) can be expressed by the curve fitting, as:

$$\omega_{wt\_ref} = 1.6{P_e}^3 - 2.7{P_e}^2 + 2.3P_e + 0.45 \tag{4}$$

Equation (4) relates the reference speed of the WT (ω_{wt_ref}) to its output electrical power. The maximum and minimum limits of the WT speed are 1.2 pu and 0.7 pu, respectively.

The droop controller is emulated by Fig. 4, which demonstrates that the temporary power signal P_{droop} is dependent on the frequency deviation (ΔF) of Area 1 ΔF_1. The droop controller performs the same function as the droop controller of the SG [3, 44], which accelerates and decelerates the rotor of type 3 WT in case of positive and negative ΔF_1, respectively [45].

The pitch angle controller, which avoids the output power corresponding to higher wind speed exceeding the generator rated power, is illustrated in Fig. 5. The dependent WT speed deviation signal β_{ref} is the required pitch angle to avoid the speed of the rotor exceeding its limits. β_{ref} is zero during normal wind speed, but for wind speed above the rated value, it has a value higher than zero. β_a is an additional signal which is used to increase and decrease WT output power during negative and positive ΔF, respectively [45]. P_{droop} and β are the outputs of Figs. 4 and 5, which are the VSWT model inputs in Fig. 2.

2.2 Model of PV

Panels of PV consist of a few PV modules which are connected in parallel and in series to increase the current and voltage of the PV array [24]. The mathematical equations which describe the PV model are given in (5)–(10) [46], while the required PV parameters for electrical characteristic simulation are given in Table 1 [47].

$$V_t = \frac{K_{Bz}T}{Q_e} \tag{5}$$

$$I_{ph} = \left(\frac{G}{G_{ref}}\right)\left(I_{phn} + K_i\left(T - T_{ref}\right)\right) \tag{6}$$

$$I_o = I_{sc}\left(\frac{G}{G_{ref}}\right)\left(\frac{T}{T_{ref}}\right)^3 e^{\left(1-\frac{V_{oc}}{MV_t}\right)} \tag{7}$$

$$I_{PV} = I_{ph} - \left(\frac{I_{PV}R_s + V_{PV}}{R_P}\right) - I_o\left(e^{\left(\frac{I_{PV}R_s+V_{PV}}{MV_t}\right)} - 1\right) \tag{8}$$

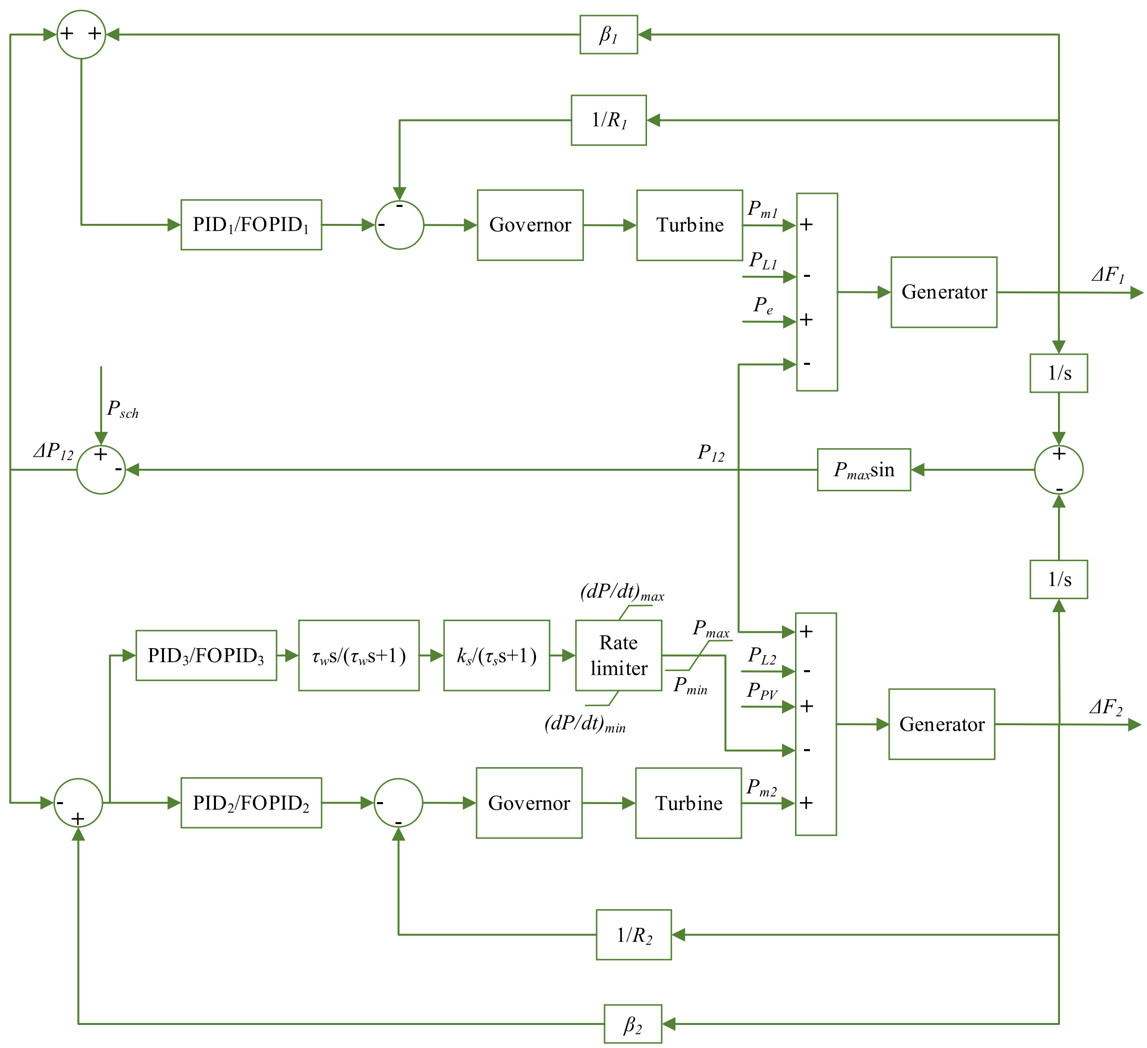

Fig. 1 Block diagram model of the studied two-area power system

$$R_P = R_{Ps}\left(\frac{G}{G_{ref}}\right) \tag{9}$$

$$P_{PV} = V_{PV} I_{PV} \tag{10}$$

where V_t is the thermal PV voltage, K_{Bz} is the Boltzmann constant, T is the temperature of the PV, Q_e is the electron charge, and G is the actual irradiance. G_{ref} and T_{ref} are the irradiance and temperature at standard conditions, respectively. K_i is the short circuit current temperature coefficient, I_{ph} and I_{phn} are the respective light produced current at the actual temperature and at standard conditions, I_o is the reverse saturation diode current, and I_{sc} is the short circuit current. V_{oc} is the open circuit voltage, M is the factor of diode ideality, I_{PV} is the PV output current, V_{PV} is the PV output voltage, R_P is the shunt resistance, R_s is the series resistance, R_{Ps} is the standard condition shunt resistance, and P_{PV} is the output power of the PV.

MPPT methods are required for bulk stations of PV [48]. Reference [49] illustrates a comprehensive review on various MPPT methods for PV. An artificial neural network (ANN) for MPPT as discussed in [50] is used in this paper. There are two input layers (T, G) and one output layer (V_{PV}). The output current and power at MPP are detected once the MPPT voltage is estimated.

2.3 Model of conventional units

Hydro and steam power plants are incorporated into the proposed two-area power system. The transfer functions of the steam turbine are modelled mathematically as:

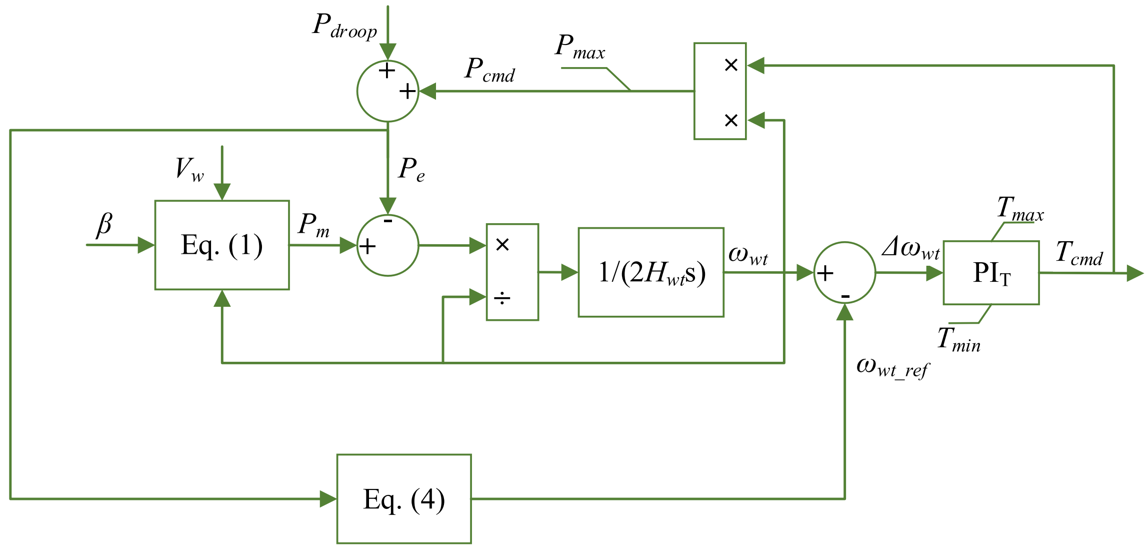

Fig. 2 Block diagram model of the proposed type 3 wind turbine

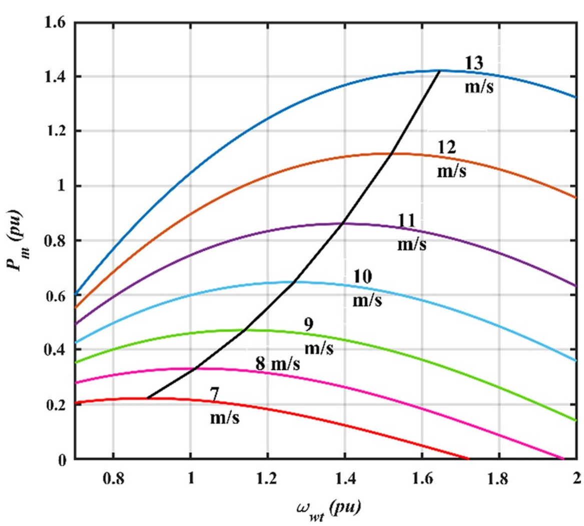

Fig. 3 Output mechanical power of the proposed type 3 wind turbine at certain rotational speed for different wind speeds

$$\text{Turbine model} \quad \frac{F_{HP}T_{RH}s+1}{(T_{RH}s+1)(T_{CH}s+1)}$$

$$\text{Governor model} \quad \frac{1}{T_G s+1}$$

$$\text{Generator model} \quad \frac{1}{2H_1 s+D_1}$$

The steam turbine model is based on a single reheat stage as described in [51]. T_{RH} and T_{CH} represent the reheater and main inlet valve time constants, and F_{HP} is the fractional power generated by the high-pressure turbine. The time lag of the governor is represented by the time constant T_G. The generator model is represented by its swing equation where H_1 represents its inertia and D_1 is the load damping constant.

The transfer functions of the hydro turbine are modelled as:

$$\text{Turbine model} \quad \frac{-T_W s+1}{0.5T_W s+1}$$

$$\text{Governor model} \quad \frac{T_R s+1}{(T_{GH}s+1)\left(\left(\frac{R_{Td}}{R_{Pd}}\right)T_R s+1\right)}$$

$$\text{Generator model} \quad \frac{1}{2H_2 s+D_2}$$

The model of the hydro turbine is a non minimum phase system that represents the change in output power due to the change in gate opening, and T_W represents the water starting time. Unlike a steam turbine governor, a hydro turbine governor requires an additional transient droop with long resetting time to limit the gate movement until water flow and output power have time to catch up [51]. R_{Pd} represents the permanent droop and R_{Td} is the transient droop, T_R is the reset time, and T_{GH} is a time constant representing the delay in the governor response. Also, the generator model is represented by its swing equation where H_2 represents its inertia and D_2 is the load damping constant.

Table 1 Parameters of the proposed two-area power system

Area 1		Area 2	
Parameters	**Value**	**Parameters**	**Values**
H_1	3 s	H_2	3 s
D_1	1 pu	D_2	1 pu
R_1	0.05 pu	R_2	0.05 pu
β_1	21 pu	β_2	21 pu
F_{HP}	0.3	T_W	1 s
T_{RH}	7 s	T_R	0.513 s
T_{CH}	0.3 s	T_{GH}	48.7 s
T_G	0.2 s	R_{Td}/R_{Pd}	19.493
Type 3 wind turbine		PV	
H_{wt}	5.74 s	R_s	0.134 Ω
PI_T	$k_p = 3$	R_{Ps}	134.48 Ω
	$k_i = 0.3$	I_{phn}	8.2527 A
P_{max}	3.6 MW	M	1.282
T_{min}	0	T_{ref}	25 °C
T_{max}	0.833 pu	G_{ref}	$1000 W/m^2$
Pitch angle and droop controller		I_{sc}	8.2 A
Delay	0.1 s	V_{oc}	33.12 V
Dead zone	0.001 pu	K_i	0.037%/°C
$P_{droop,min}$	−0.2 pu	V_{MPP}	27.28 V
$P_{droop,max}$	0.2 pu	I_{MPP}	7.5 A
PI_P	$k_p = 50$	P_{MPP}	204.6 W
	$k_i = 4.5$	Auxiliary storage	
$\beta_{a,min}$	−10 degrees	K_s	0.98 pu
$\beta_{a,max}$	10 degrees	τ_s	0.03 s
τ_d	0.3 s	$(dP/dt)_{min}$	−0.1 pu/s
β_{min}	0 degree	$(dP/dt)_{max}$	0.1 pu/s
β_{max}	27 degrees	P_{min}	− 0.1 pu
$(d\beta/dt)_{min}$	−10 degrees/s	P_{max}	0.1 pu
$(d\beta/dt)_{max}$	10 degrees/s		

The values H_1 and H_2 are given at zero penetration of RES

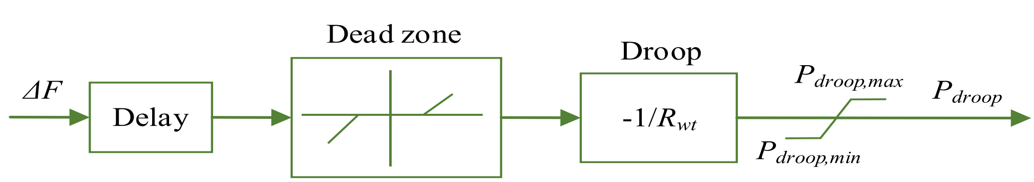

Fig. 4 Droop controller of the proposed type 3 wind turbine

3 Coot optimization algorithm

COA is categorized as a novel swarm-based meta-heuristic algorithm, introduced by Iraj Naruei and Farshid Keynia [52]. Its behavior for food seeking can be described by the following four phases: random motion; chain motion; improving coot position by tracing the leaders; and leader motion toward optimal zone including the food. The algorithm is started by selecting an initial population randomly, and this population is frequently estimated by the objective function until the optimal value is obtained. The randomly generated population can be evaluated as:

$$coot\ position(i) = Rand(1, dim) \times (UB - LB) + LB \tag{11}$$

$$LB = LB_1, LB_2, LB_3, \ldots, LB_{dim} \tag{12}$$

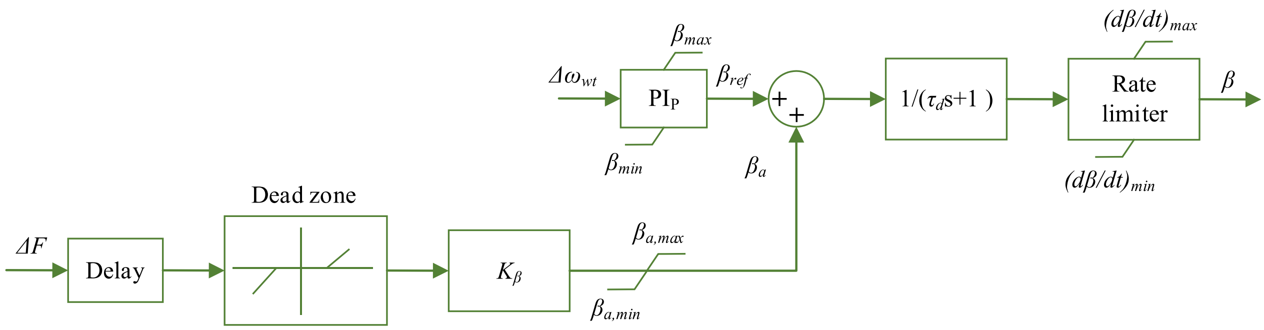

Fig. 5 Pitch angle controller of the proposed type 3 wind turbine

$$UB = UB_1, UB_2, UB_3, \ldots, UB_{dim} \tag{13}$$

where i is the current coot index, $coot\,position(i)$ is the position of coot, dim is the dimension of the problem, LB is the lower bound matrix and UB is the upper bound matrix.

The fitness of each coot is calculated by the objective function after determining the coot initial population and position. The objective function which is required to be optimized by COA is given in (14), which represents the integral square error (ISE) consisting of three small values of tie line power deviation (ΔP_{12}), and the deviations in frequency of Area 1 (ΔF_1) and Area 2 (ΔF_2).

$$ISE = \int_0^t \left(\Delta P_{12}{}^2 + \Delta F_1{}^2 + \Delta F_2{}^2 \right) dt \tag{14}$$

The random motion of a coot which helps the algorithm to explore various zones in the search space and converge to the global optimum is illustrated in (15), and the new coot position is estimated in (16).

$$Q = Rand(1, dim) \times (UB - LB) + LB \tag{15}$$

$$\begin{aligned} coot\,position(i) =& coot\,position(i) + A \times R_1 \\ & \times (Q - coot\,position(i)) \end{aligned} \tag{16}$$

where R_1 is a random number between [0,1] and A is estimated by:

$$A = 1 - \frac{Iter}{Iteration} \tag{17}$$

where the maximum iteration number is represented by $Iteration$ and the current iteration is represented by $Iter$.

The second phase is the chain movement which can be implemented by calculating the mean position of two coots as:

$$\begin{aligned} coot\,position(i) =& 0.5 \times (coot\,position(i-1) \\ & + coot\,position(i)) \end{aligned} \tag{18}$$

where $coot\,position(i-1)$ is the position of the second coot.

Improving the position of coots by tracing leaders can be implemented by selecting a few leaders randomly and estimating their mean position. Then coots modify their positions according to the mean position of the leaders. The criteria for leader selection is provided in (19) and the modified coot position according to leader position is estimated according to (20).

$$K = 1 + (iMODLD) \tag{19}$$

$$\begin{aligned} coot\,position(i) =& LDP(K) + 2 \times R_2 \times cos\,(2R\pi) \\ & \times (LDP(K) - coot\,position(i)) \end{aligned} \tag{20}$$

where K is the index number of the leader, LD is the number of leaders, R_2 is a random number between [0,1], R is a random number between [−1,1] and $LDP(K)$ is the chosen leader position.

Finally, leaders' position is modified to find a new optimal point near the best position that has been found, as:

$$LDP(i) = \begin{cases} B \times R_3 \times cos(2R\pi) \times (GB - LDP(i)) + GB, R_4 < 0.5 \\ B \times R_3 \times cos(2R\pi) \times (GB - LDP(i)) - GB, R_4 \geq 0.5 \end{cases} \tag{21}$$

where R_3 and R_4 are random numbers between [0,1], GB is the best position and B is estimated by:

$$B = 2 - \frac{Iter}{Iteration} \tag{22}$$

$B \times R_3$ prevents the COA from blocking in a local optimum by performing larger movements randomly, which means that the COA performs exploitation and exploration at the same time. On the other hand, $cos(2R\pi)$ helps to seek a better position near the best-found position with various radii. Figure 6 illustrates the flow chart which demonstrates the procedures of COA.

4 Simulation results

This section illustrates various scenarios that are performed on the proposed system discussed earlier in Sect. 2. These scenarios are illustrated by MATLAB/SIMULINK 2018b. Optimization processes are applied on the 1st and 2nd scenarios for COA benchmarking and comparisons. COA results are validated in the 3rd and 4th scenarios.

For fair comparison, lower bound, upper bound and the number of populations are maintained constant for all optimizers and the number of iterations is selected as 100.

4.1 Scenario 1: optimization of conventional PID controller parameters

In this scenario, optimization is performed to allocate the optimal parameters of PID controllers, time of washout filter (τ_W), pitch angle controller gain (K_β) and WT droop (R_{wt}). The objective function of the *ISE* is optimized for 100 s by the 5 optimizers, i.e.: PSO, WCA, HBA, AOS and COA. It is found that the corresponding *ISE* are 2.6307×10^{-5}, 3.1371×10^{-5}, 3.3435×10^{-5}, 5.1316×10^{-5} and 5.3451×10^{-5} for COA, AOS, HBA, WCA and PSO, respectively. The convergence curves of the 5 optimizers for 100 iterations are shown in Fig. 7. Optimal settings of the optimized parameters for the 5 optimizers are demonstrated in Table 2, while the system responses ΔF_1, ΔF_2 and ΔP_{12} due to 0.05 pu load increase in Area 1 are illustrated in Fig. 8. The maximum deviations in ΔF_1, ΔF_2 and ΔP_{12} in the case of COA are -1.97×10^{-3} pu, -7.4×10^{-4} pu and -4.13×10^{-3} pu, respectively. It is also found that the maximum deviation in ΔF_1 in case the of COA is less than WCA by 72.6% while the maximum deviation in ΔF_2 in COA is less than PSO and WCA by 20.27% and 32.43%, respectively. In addition, the maximum deviation in ΔP_{12} in the case of COA is less than PSO, WCA, HBA and AOS by 30.5%, 69.98%, 5.09% and 3.9%, respectively. It proves that *ISE* for COA is the smallest of the optimizers. The reductions in the maximum deviations of ΔF_1, ΔF_2 and ΔP_{12} in the case of COA are greater than other optimizers. The overall conclusion is that COA is the most robust of the optimizers for PID controllers.

4.2 Scenario 2: optimization of FOPID controller parameters

In this scenario, PID controllers are replaced by FOPID controllers and optimization is performed to allocate the optimal parameters of these controllers in addition to τ_W,K_β and R_{wt}. It is found that *ISE* are 1.8708×10^{-5}, 2.3697×10^{-5}, 3.2711×10^{-5}, 3.7009×10^{-5} and 4.7540×10^{-5} for COA, AOS, HBA, PSO and WCA, respectively. The convergence curves of the 5 optimizers for 100 iterations are shown in Fig. 9. Optimal settings of the optimized parameters for the 5 optimizers are demonstrated in Table 3, and the system responses ΔF_1, ΔF_2 and ΔP_{12} due to 0.05 pu load increase in Area 1 are illustrated in Fig. 10. As seen, the maximum deviations in ΔF_1, ΔF_2 and ΔP_{12} in the case of COA are -2.79×10^{-3} pu, -6.7×10^{-4} pu and -3.7×10^{-3} pu, respectively. It is found that the maximum deviation in ΔF_1 in the case of COA is less than PSO and WCA by 4.3% and 21.15%, respectively, while the maximum deviation in ΔF_2 for the COA is less than PSO, HBA and AOS by 5.97%, 44.78% and 25.37%, respectively. Also, the maximum deviation in ΔP_{12} for the COA is less than PSO, WCA, HBA and AOS by 28.1%, 80.27%, 51.08% and 0.54%, respectively. It proves that *ISE* for the COA is the smallest of the optimizers. Moreover, the reductions in the maximum deviations of ΔF_1, ΔF_2 and ΔP_{12} in the case of the COA are greater than the others. In addition, *ISE* in this scenario are smaller than *ISE* in the 1st scenario. Thus, it can be concluded that the COA is the most robust optimizer for FOPID controller when compared to the other four optimizers and PID. The advantage of FOPID over the conventional PID can be considered as FOPID having more optimized parameters than conventional PID. Thus, FOPID is included in the next two scenarios for further investigation.

4.3 Scenario 3: robustness of the COA under variable load disturbances

In this scenario, the COA is validated (including FOPID) under various load disturbances in Area 1 which are shown in Fig. 11. It is observed that *ISE* are 2.7045×10^{-4}, 3.7125×10^{-4}, 4.4567×10^{-4}, 3.3989×10^{-4} and 4.1807×10^{-4} for COA, AOS, HBA, PSO and WCA, respectively. The system responses ΔF_1, ΔF_2 and ΔP_{12} due to various load disturbances (shown in Fig. 11) are illustrated in Fig. 12. Looking at the deviations in the case of COA, the maximum deviations in ΔF_1 are -2.79×10^{-3} pu, 5.28×10^{-3} pu and -5.36×10^{-3} pu for the 1st, 2nd and 3rd disturbances, respectively. The maximum deviations in ΔF_2 are -6.7×10^{-4} pu, 1.183×10^{-3} pu and -1.24×10^{-3} pu for the 1st, 2nd and 3rd disturbances respectively. Also, the maximum deviations in ΔP_{12} are -3.7×10^{-3} pu, 8.47×10^{-3} pu and -7.97×10^{-3} pu for the 1st, 2nd and 3rd disturbances, respectively. The percentage reductions in ΔF_1, ΔF_2 and ΔP_{12} compared to others are shown in Table 4. It can be seen that *ISE* for COA are the smallest. For COA, the reductions in the maximum deviations of ΔF_1, ΔF_2 and ΔP_{12} are greater than other optimizers (Table 4). Thus, the overall conclusion is that COA is the most robust and

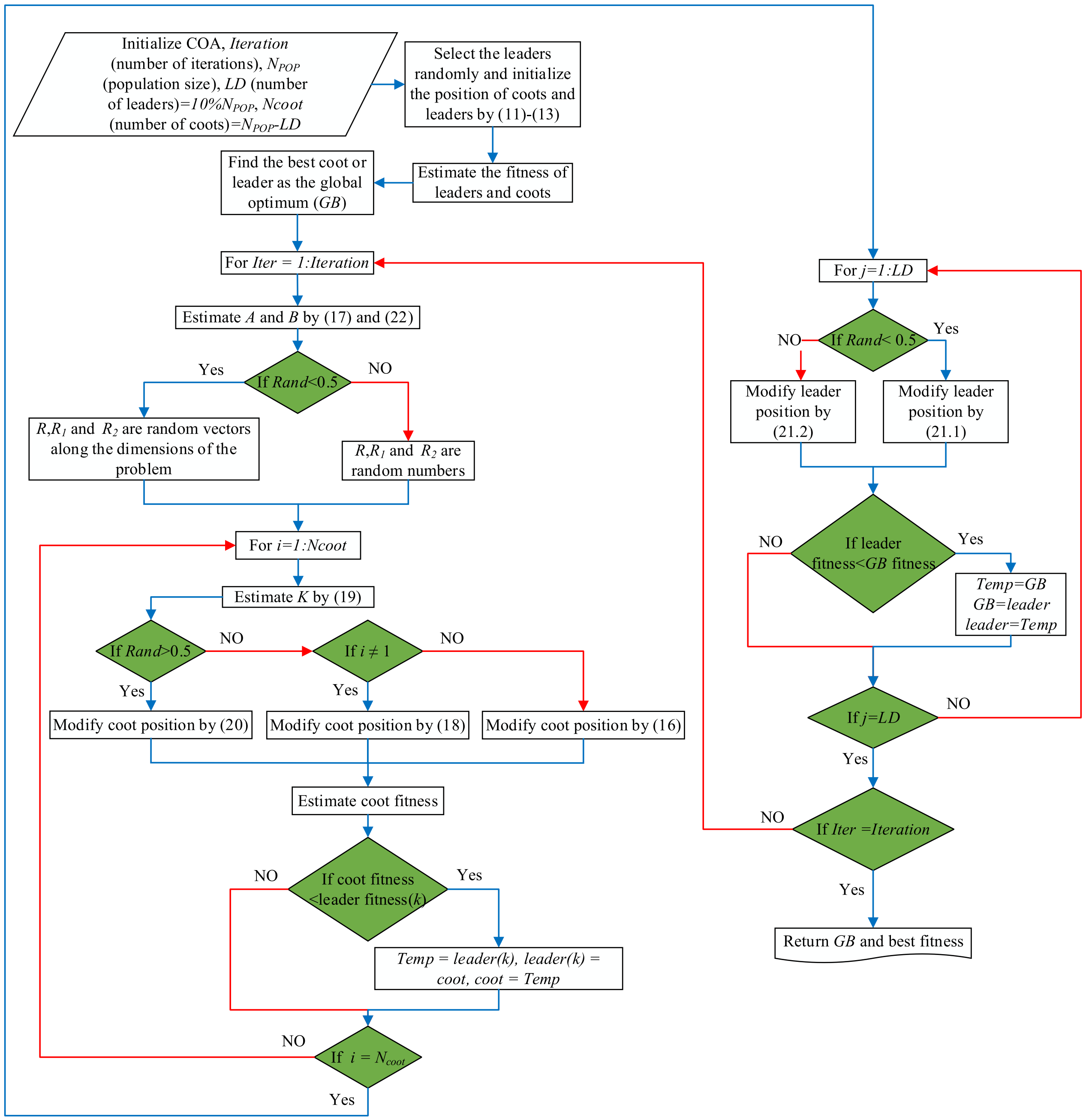

Fig. 6 Flowchart of COA optimizer

benchmarked optimizer. COA is tested in the next scenario in real weather conditions.

4.4 Scenario 4: robustness of COA in varying weather conditions

Here, COA is validated (including FOPID) using real measurements at Zafarana in Egypt [35] for temperature, irradiance and wind speed. Four-day samples of temperature, irradiance and wind speed are recorded in Fig. 13, and the system responses ΔF_1, ΔF_2 and ΔP_{12} due to real weather data are illustrated in Fig. 14. The maximum deviation in frequency for the two-area power system is −0.001281 pu (−0.06405 Hz) which is a secure value according to the operation of the under frequency load shedding relays [53]. It can be seen that the system behaves satisfactorily in real weather conditions. Thus,

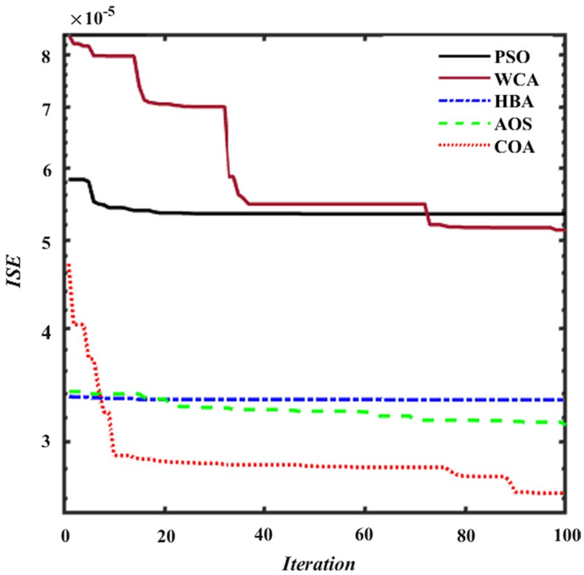

Fig. 7 Comparison of ISE convergence for the five used optimizers of the two-area power system including PID controllers

Table 2 Parameters of PID controllers

Parameter	PSO	WCA	HBA	AOS	COA
K_{P1}	−1.5710	−2.5854	−3.0000	−3.0000	−3.0000
K_{d1}	−2.9629	−0.6201	−3.0000	−3.0000	−2.8049
K_{i1}	−2.5130	−2.7656	−3.0000	−3.0000	−2.9959
K_{P2}	−1.2623	−1.6248	−3.0000	−3.0000	−0.4804
K_{d2}	−2.0399	−1.3508	−3.0000	−3.0000	−2.7286
K_{i2}	−0.8412	−0.6896	−0.4000	−0.5696	−0.53057
K_{P3}	−2.8177	−0.8436	−3.0000	−3.0000	−2.3027
K_{d3}	−1.0046	−0.9239	−3.0000	−1.8042	−0.4000
K_{i3}	−2.4193	−2.8433	−3.0000	−3.0000	−2.9397
τ_W	29.7104	7.3959	30.0000	30.0000	14.7056
K_β	27.1451	18.0232	41.7032	50.0000	10.0000
R_{wt}	0.1745	0.2006	0.3000	0.1686	0.101994

COA proves its robustness and can be a promising and benchmarked optimizer.

In summary of the performance of COA and from the optimization results of PID controllers, we see that COA gives the best objective function. In addition, COA gives the best fitness function for the optimization of FOPID controllers. The fitness function of FOPID is 28.88% less than that of PID because the FOPID controller has more decision parameters and hence a higher degree of freedom. Therefore, FOPID is included in the validation and benchmarking scenarios. COA also shows its robustness under variable stiff load disturbances in the 3rd scenario,

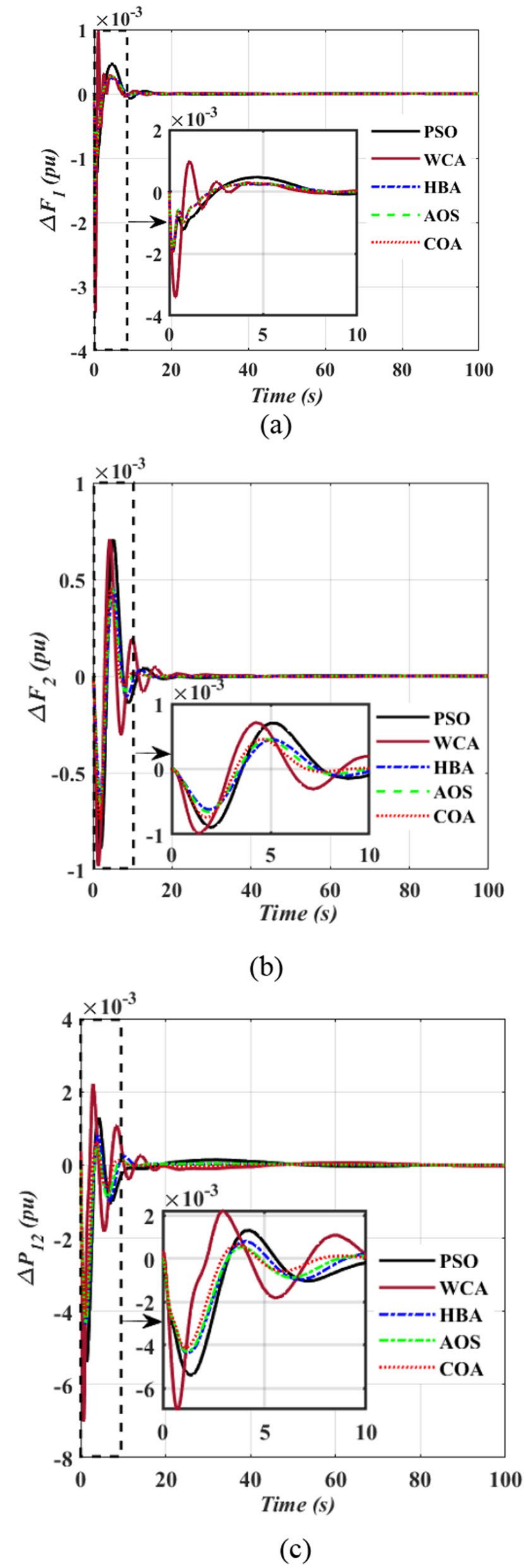

Fig. 8 System responses due to +0.05 pu step load change in Area 1 while including PID controller **a** ΔF_1, **b** ΔF_2, **c** ΔP_{12}

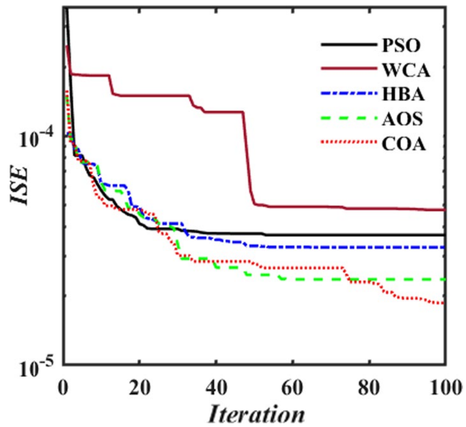

Fig. 9 Comparison of ISE convergence for the five optimizers of the two-area power system including FOPID controllers

Table 3 Optimal parameters of FOPID controllers

Parameters	PSO	WCA	HBA	AOS	COA
K_{P1}	−2.2754	−3.0000	−3.0000	−2.8961	−2.9923
K_{d1}	−2.9885	−1.0941	−0.4974	−2.5512	−2.9951
K_{i1}	−2.1337	−2.6009	−3.0000	−2.0296	−2.9963
λ_1	1.1628	1.1499	0.6951	1.1039	0.8981
μ_1	0.5785	0.6957	1.5000	0.8235	0.6212
K_{P2}	−2.0994	−1.7360	−0.4000	−2.0270	−1.5198
K_{d2}	−2.2324	−3.0000	−3.0000	−0.8984	−2.0910
K_{i2}	−1.1722	−0.6284	−0.4201	−1.5313	−1.5401
λ_2	1.0357	1.0972	0.9776	1.0640	0.9851
μ_2	1.2783	1.3344	1.5000	0.8986	0.8889
K_{P3}	−2.2041	−2.7547	−3.0000	−2.6479	−1.7242
K_{d3}	−1.8897	−3.0000	−0.4017	−0.4000	−1.3896
K_{i3}	−2.3044	−2.2270	−3.0000	−2.4039	−2.9688
λ_3	0.9339	1.1775	0.7186	0.8567	0.7946
μ_3	0.9786	0.9378	1.5000	1.3548	1.0835
τ_W	18.7768	25.0082	30.0000	28.8367	14.7073
K_β	23.6464	33.2494	50.0000	46.8303	19.4407
R_{wt}	0.2149	0.1992	0.1000	0.1895	0.2110

while it also behaves satisfactorily in real weather conditions in the 4th scenario.

In the studied cases, COA optimizer behaves better than other optimizers. This is because COA has four different coots moving strategies on the water surface: random to this side and that side; chain movement; movement adjustment according to the leader; and leader movement. The random movement helps to explore the search space, while the algorithm has immunity to being stuck in local minima by updating the new position, as

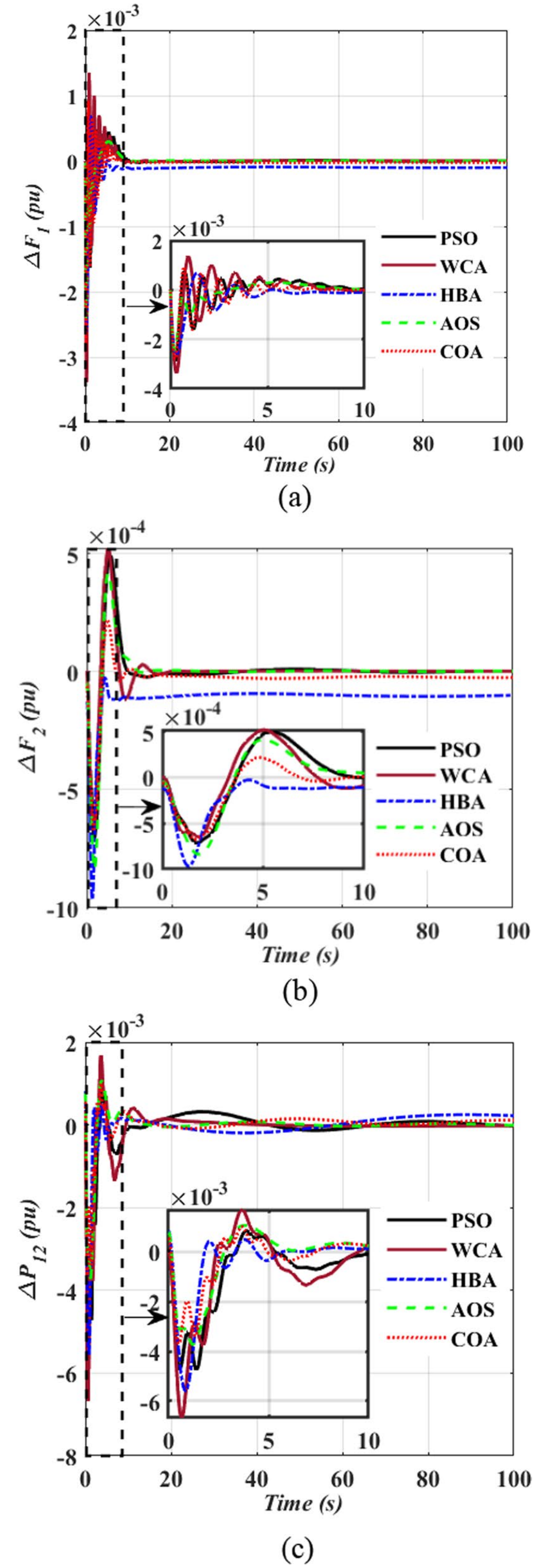

Fig. 10 System responses due to +0.05 pu step load change in Area 1 while including FOPID controller **a** ΔF_1, **b** ΔF_2, **c** ΔP_{12}

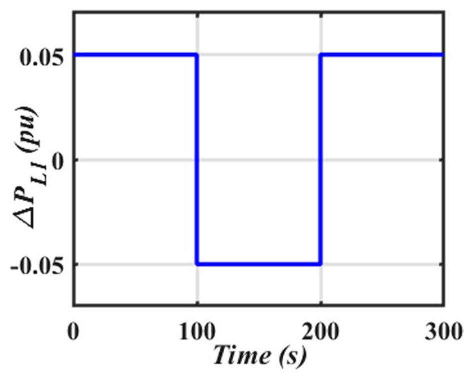

Fig. 11 Variable step load change in Area 1

described by (16). Extensive movement toward the optimum area are assured by the leader's movement. The coots may move in a chain or toward group leaders randomly, and this helps to preserve the random nature of the algorithm.

5 Conclusion

In this paper, an efficient LFC has been performed on a two-area power system using robust FOPID controllers. This two-area power system contains steam and hydro generators integrated with a high penetration of RES such as PV panels and WTs. The five optimal parameters of the FOPID controllers which satisfy the best value of *ISE* are obtained by the COA. The robustness of the COA is validated through four scenarios with comparisons to other benchmarked optimizers including PSO, WCA, HBA and AOS. Optimization is first performed while including traditional PID controllers and the results confirm that the COA results in the smallest *ISE*. The results of the 1st scenario show that *ISE* with COA is less than AOS, HBA, WCA and PSO by 20.01%, 27.86%, 95.8% and 103.94%, respectively. Then, optimization is performed while traditional PID controllers are replaced by FOPID controllers. The results of the optimization shed light on the robustness of FOPID controllers based on the COA approach. The results of the 2nd scenario show that *ISE* with COA is less than AOS, HBA, PSO and WCA by 26.67%, 74.85%, 97.82% and 154.12%, respectively. In the 3rd scenario, the system responses are observed while the two-area power system is subjected to variable load disturbances. The results illustrate that *ISE* with COA is less than PSO, AOS, WCA and HBA by 25.68%, 37.3%, 54.58% and 64.8%, respectively. Finally, the performance assessment of FOPID optimized by the COA is examined in real weather conditions. This results in a maximum frequency deviation of −0.06405 Hz. The results illustrate the efficiency and applicability of the proposed FOPID controllers based on a COA approach.

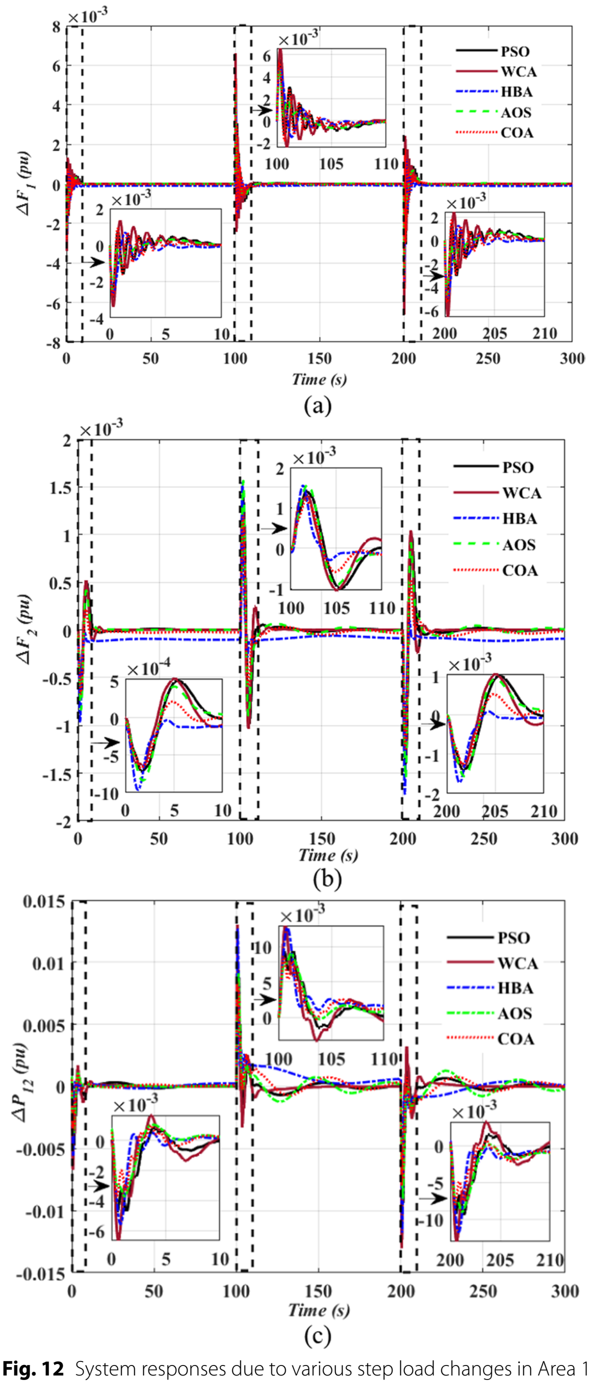

Fig. 12 System responses due to various step load changes in Area 1 while including FOPID controller **a** ΔF_1, **b** ΔF_2, **c** ΔP_{12}

Table 4 Reductions in ΔF_1, ΔF_2 and ΔP_{12} deviations due to 3 step load changes using COA

Optimizer	ΔF_1			ΔF_2			ΔP_{12}		
	1st (%)	2nd (%)	3rd (%)	1st (%)	2nd (%)	3rd (%)	1st (%)	2nd (%)	3rd (%)
PSO	4.30	6.16	4.48	5.97	19.53	14.52	28.10	10.23	16.73
WCA	21.15	25.02	23.13	–	10.48	4.84	80.27	53.42	63.49
HBA	–	–	–	44.78	30.85	38.71	51.08	49.99	47.68
AOS	–	–	–	25.37	32.29	25.81	0.54	7.38	12.92

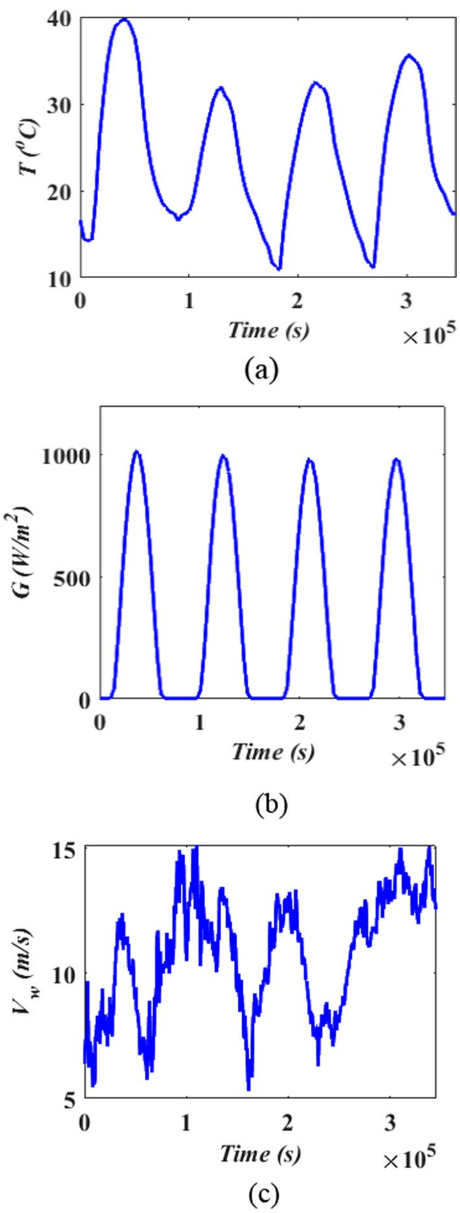

Fig. 13 Real weather conditions at Zafarana **a** T, **b** G, **c** V_w

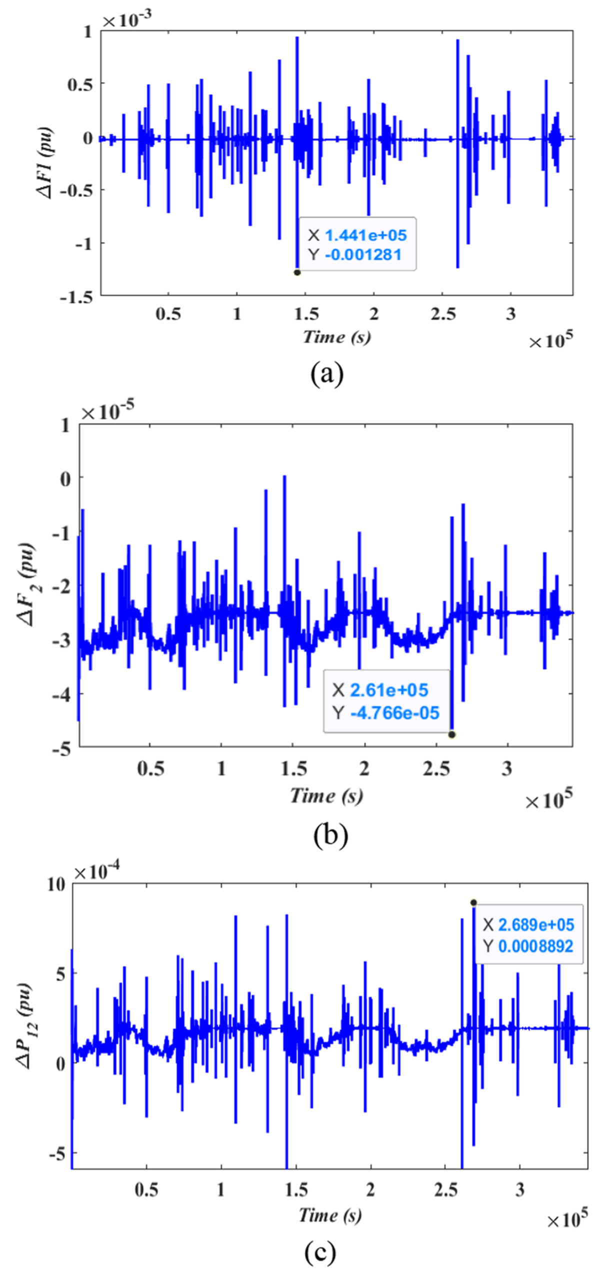

Fig. 14 System responses due to real weather conditions **a** ΔF_1, **b** ΔF_2, **c** ΔP_{12}

Abbreviations

RES	Renewable energy sources
SG	Synchronous generator
BES	Battery energy storage
WT	Wind turbine
SMES	Superconducting magnetic energy storage
SCES	Supercapacitor energy storage
VSWT	Variable speed wind turbine
LFC	Load frequency control
PID	Proportional integral derivative
FWES	Flywheel energy storage
EV	Electric vehicle
FOPID	Fractional-order proportional integral derivative
PSO	Particle swarm optimization
COA	Coot optimization algorithm
AOS	Atomic orbital search
HBA	Honey badger algorithm
WCA	Water cycle algorithm
MPPT	Maximum power point tracking
ANN	Artificial neural network

Acknowledgements
Not applicable.

Author contributions
Each author contributed significantly to the implementation of the proposed work. All authors read and approved the final manuscript.

Funding
Not applicable.

Availability of data and materials
All data used or analyzed during this study are included in the manuscript.

Declarations

Competing interests
The authors declare that they have no known competing financial interests or personal relationships that could have appeared to influence the work reported in this paper.

Received: 1 August 2022 Accepted: 27 March 2023
Published online: 06 April 2023

References

1. Robles, E., Haro-Larrode, M., Santos-Mugica, M., Etxegarai, A., & Tedeschi, E. (2019). Comparative analysis of european grid codes relevant to offshore renewable energy installations. *Renewable and Sustainable Energy Reviews*, *102*, 171–185. https://doi.org/10.1016/j.rser.2018.12.002.
2. Tang, Z. X., Lim, Y. S., Morris, S., Yi, J. L., Lyons, P. F., & Taylor, P. C. (2019). A comprehensive work package for energy storage systems as a means of frequency regulation with increased penetration of photovoltaic systems. *International Journal of Electrical Power & Energy Systems*, *110*, 197–207. https://doi.org/10.1016/j.ijepes.2019.03.002.
3. Fernández-Guillamón, A., Gómez-Lázaro, E., Muljadi, E., & Molina-García, Á. (2019). Power systems with high renewable energy sources: A review of inertia and frequency control strategies over time. *Renewable and Sustainable Energy Reviews*, *115*, 109369. https://doi.org/10.1016/j.rser.2019.109369.
4. Fini, M. H., & Golshan, M. E. H. (2019). Frequency control using loads and generators capacity in power systems with a high penetration of renewables. *Electric Power Systems Research*, *166*, 43–51. https://doi.org/10.1016/j.epsr.2018.09.010.
5. Akram, U., Nadarajah, M., Shah, R., & Milano, F. (2020). A review on rapid responsive energy storage technologies for frequency regulation in modern power systems. *Renewable and Sustainable Energy Reviews*, *120*, 109626. https://doi.org/10.1016/j.rser.2019.109626.
6. Sebastián, R. (2016). Application of a battery energy storage for frequency regulation and peak shaving in a wind diesel power system. *IET Generation Transmission & Distribution*, *10*(3), 764–770. https://doi.org/10.1049/iet-gtd.2015.0435.
7. Turk, A., Sandelic, M., Noto, G., Pillai, J. R., & Chaudhary, S. K. (2019). Primary frequency regulation supported by battery storage systems in power system dominated by renewable energy sources. *The Journal of Engineering, 18*, 4986–4990. https://doi.org/10.1049/joe.2018.9349
8. Magdy, G., Mohamed, E. A., Shabib, G., Elbaset, A. A., & Mitani, Y. (2018). SMES based a new PID controller for frequency stability of a real hybrid power system considering high wind power penetration. *IET Renewable Power Generation*, *12*(11), 1304–1313. https://doi.org/10.1049/iet-rpg.2018.5096.
9. Zargar, M. Y., Mufti, M. U. D., & Lone, S. A. (2017). Adaptive predictive control of a small capacity SMES unit for improved frequency control of a wind-diesel power system. *IET Renewable Power Generation*, *11*(14), 1832–1840. https://doi.org/10.1049/iet-rpg.2017.0074.
10. Jami, M., Shafiee, Q., Gholami, M., & Bevrani, H. (2020). Control of a supercapacitor energy storage system to mimic inertia and transient response improvement of a direct current micro-grid. *Journal of Energy Storage*, *32*, 101788. https://doi.org/10.1016/j.est.2020.101788.
11. Singh, K. (2021). Enhancement of frequency regulation in tidal turbine power plant using virtual inertia from capacitive energy storage system. *Journal of Energy Storage*, *35*, 102332. https://doi.org/10.1016/j.est.2021.102332.
12. Yan, G., Liang, S., Jia, Q., & Cai, Y. (2019). Novel adapted de-loading control strategy for PV generation participating in grid frequency regulation. *The Journal of Engineering*, *2019*(16), 3383–3387. https://doi.org/10.1049/joe.2018.8481.
13. Zarina, P., Mishra, S., & Sekhar, P. (2012). Deriving inertial response from a non-inertial PV system for frequency regulation. In *2012 IEEE international conference on power electronics, drives and energy systems (PEDES)* (pp. 1–5.) https://doi.org/10.1109/PEDES.2012.6484409
14. Li, M., & Wang, Y. (2020). Research of frequency coordinated Control Strategy based on variable de-loading level for D-PMSG wind turbine. *Journal of Electrical Engineering & Technology*, *15*(6), 2563–2576. https://doi.org/10.1007/s42835-020-00552-0.
15. Vidyanandan, K., & Senroy, N. (2012). Primary frequency regulation by deloaded wind turbines using variable droop. *IEEE transactions on Power Systems*, *28*(2), 837–846. https://doi.org/10.1109/TPWRS.2012.2208233.
16. Zhang, X., Zha, X., Yue, S., & Chen, Y. (2018). A frequency regulation strategy for wind power based on limited over-speed de-loading curve partitioning. *IEEE Access: Practical Innovations, Open Solutions*, *6*, 22938–22951. https://doi.org/10.1109/ACCESS.2018.2825363.
17. Morren, J., De Haan, S. W., Kling, W. L., & Ferreira, J. (2006). Wind turbines emulating inertia and supporting primary frequency control. *IEEE Transactions on Power Systems*, *21*(1), 433–434. https://doi.org/10.1109/TPWRS.2005.861956.
18. Zhang, W., & Fang, K. (2017). Controlling active power of wind farms to participate in load frequency control of power systems. *IET Generation Transmission & Distribution*, *11*(9), 2194–2203. https://doi.org/10.1049/iet-gtd.2016.1471.
19. Su, C., & Chen, Z. (2012). Influence of wind plant ancillary frequency control on system small signal stability. In *2012 IEEE power and energy society general meeting* (pp. 1–8). https://doi.org/10.1109/PESGM.2012.6345411
20. Zhang, Z., Wang, Y., Li, H., & Su, X. (2013). Comparison of inertia control methods for DFIG-based wind turbines. In 2013 *IEEE ECCE Asia Downunder*, 2013 (pp. 960–964). https://doi.org/10.1109/ECCE-Asia.2013.6579222
21. El-Hameed, M. A., Elkholy, M. M., & El-Fergany, A. A. (2019). Efficient frequency regulation in highly penetrated power systems by renewable energy sources using stochastic fractal optimiser. *IET Renewable Power Generation*, *13*(12), 2174–2183. https://doi.org/10.1049/iet-rpg.2019.0186.
22. Hwang, M., Muljadi, E., Park, J. W., Sørensen, P., & Kang, Y. C. (2016). Dynamic droop–based inertial control of a doubly-fed induction generator. *IEEE Transactions on Sustainable Energy*, *7*(3), 924–933. https://doi.org/10.1109/TSTE.2015.2508792.
23. Van de Vyver, J., De Kooning, J. D., Meersman, B., Vandevelde, L., & Vandoorn, T. L. (2015). Droop control as an alternative inertial response strategy for the synthetic inertia on wind turbines. *IEEE Transactions on*

Power Systems, *31*(2), 1129–1138. https://doi.org/10.1109/TPWRS.2015.2417758.
24. Fathy, A., Yousri, D., Rezk, H., Thanikanti, S. B., & Hasanien, H. M. (2022). A Robust Fractional-Order PID Controller based load frequency control using modified Hunger Games search optimizer. *Energies*, *15*(1), 361. https://doi.org/10.3390/en15010361.
25. Wang, L., Yu, J. Y., & Chen, Y. T. (2011). Dynamic stability improvement of an integrated offshore wind and marine-current farm using a flywheel energy-storage system. *IET Renewable Power Generation*, *5*(5), 387–396. https://doi.org/10.1049/iet-rpg.2010.0194.
26. Abazari, A., Monsef, H., & Wu, B. (2019). Load frequency control by de-loaded wind farm using the optimal fuzzy-based PID droop controller. *IET Renewable Power Generation*, *13*(1), 180–190. https://doi.org/10.1049/iet-rpg.2018.5392.
27. Abazari, A., Ghazavi Dozein, M., Monsef, H., & Wu, B. (2019). Wind turbine participation in micro-grid frequency control through self-tuning, adaptive fuzzy droop in de-loaded area. *IET Smart Grid*, *2*(2), 301–308. https://doi.org/10.1049/iet-stg.2018.0095.
28. Gaur, P., Bhowmik, D., & Soren, N. (2019). Utilisation of plug-in electric vehicles for frequency regulation of multi-area thermal interconnected power system. *IET Energy Systems Integration*, *1*(2), 88–96. https://doi.org/10.1049/iet-esi.2018.0028.
29. Mohapatra, T. K., Dey, A. K., & Sahu, B. K. (2020). Employment of quasi oppositional SSA-based two-degree-of-freedom fractional order PID controller for AGC of assorted source of generations. *IET Generation Transmission & Distribution*, *14*(17), 3365–3376. https://doi.org/10.1049/iet-gtd.2019.0284.
30. Kazemi, M. V., Gholamian, S. A., & Sadati, J. (2020). Adaptive fractional-order control of power system frequency in the presence of wind turbine. *IET Generation, Transmission & Distribution, 14*(4), 594–605. https://doi.org/10.1049/iet-gtd.2019.0458
31. Sondhi, S., & Hote, Y. V. (2014). Fractional order PID controller for load frequency control. *Energy Conversion and Management*, *85*, 343–353. https://doi.org/10.1016/j.enconman.2014.05.091.
32. Jan, M. U., Xin, A., Abdelbaky, M. A., Rehman, H. U., & Iqbal, S. (2020). Adaptive and fuzzy PI controllers design for frequency regulation of isolated microgrid integrated with electric vehicles. *IEEE Access: Practical Innovations, Open Solutions*, *8*, 87621–87632. https://doi.org/10.1109/ACCESS.2020.2993178.
33. Ray, P. K., & Mohanty, A. (2019). A robust firefly–swarm hybrid optimization for frequency control in wind/PV/FC based microgrid. *Applied Soft Computing*, *85*, 105823. https://doi.org/10.1016/j.asoc.2019.105823.
34. Dhundhara, S., & Verma, Y. P. (2018). Capacitive energy storage with optimized controller for frequency regulation in realistic multisource deregulated power system. *Energy*, *147*, 1108–1128. https://doi.org/10.1016/j.energy.2018.01.076.
35. El-Fergany, A. A., & El-Hameed, M. A. (2017). Efficient frequency controllers for autonomous two-area hybrid microgrid system using social-spider optimiser. *IET Generation Transmission & Distribution*, *11*(3), 637–648. https://doi.org/10.1049/iet-gtd.2016.0455.
36. Pan, I., & Das, S. (2015). Fractional-order load-frequency control of interconnected power systems using chaotic multi-objective optimization. *Applied Soft Computing*, *29*, 328–344. https://doi.org/10.1016/j.asoc.2014.12.032.
37. Alqahtani, A. S., Saravanan, P., Maheswari, M., & Alshmrany, S. (2022). An automatic query expansion based on hybrid CMO-COOT algorithm for optimized information retrieval. *The Journal of Supercomputing*, *78*, 8625–8643. https://doi.org/10.1007/s11227-021-04171-y.
38. Huang, Y., Zhang, J., Wei, W., Qin, T., Fan, Y., Luo, X., & Yang, J. (2022). Research on Coverage optimization in a WSN based on an Improved COOT Bird Algorithm. *Sensors (Basel, Switzerland)*, *22*(9), 3383. https://doi.org/10.3390/s22093383.
39. Houssein, E., Hashim, H., Ferahtia, F. A., & Rezk, S., H (2022). Battery parameter identification strategy based on modified coot optimization algorithm. *Journal of Energy Storage*, *46*, 103848. https://doi.org/10.1016/j.est.2021.103848.
40. Memarzadeh, G., & Keynia, F. (2021). A new optimal energy storage system model for wind power producers based on long short term memory and coot bird search algorithm. *Journal of Energy Storage*, *44*, 103401. https://doi.org/10.1016/j.est.2021.103401.
41. Zafar, M. H., Khan, M. N., & Khan, U. A. (2021). Short term hybrid PV/Wind power forecasting for smart grid application using feedforward neural network (FNN) trained by a novel atomic orbital search (AOS) optimization algorithm. In *2021 International conference on frontiers of information technology (FIT)*, 2021 (pp. 72–77). https://doi.org/10.1109/FIT53504.2021.00023
42. Ashraf, H., Abdellatif, S. O., El-Fergany, A. A., & Elkholy, M. M. (2022). Honey badger optimizer for extracting the ungiven parameters of PEMFC model: Steady-state assessment. *Energy Conversion and Management*, *258*, 115521. https://doi.org/10.1016/j.enconman.2022.115521.
43. Clark, K., Miller, N., & Sanchez-Gasca, J. (2010). *Modeling of GE wind turbine-generators for grid studies*. Technical Report Version 4.5, General Electric Int. Inc., April 2010
44. Cheng, Y., Azizipanah-Abarghooee, R., Azizi, S., Ding, L., & Terzija, V. (2020). Smart frequency control in low inertia energy systems based on frequency response techniques: A review. *Applied Energy*, *279*, 115798. https://doi.org/10.1016/j.apenergy.2020.115798.
45. Persson, M., & Chen, P. (2017). Frequency control by variable speed wind turbines in islanded power systems with various generation mix. *IET Renewable Power Generation*, *11*(8), 1101–1109. https://doi.org/10.1049/iet-rpg.2016.0350.
46. Ghani, F., Rosengarten, G., Duke, M., & Carson, J. K. (2014). The numerical calculation of single-diode solar-cell modelling parameters. *Renewable Energy*, *72*, 105–112. https://doi.org/10.1016/j.renene.2014.06.035.
47. Ali, E. E., El-Hameed, M. A., El-Fergany, A. A., & El-Arini, M. M. (2016). Parameter extraction of photovoltaic generating units using multi-verse optimizer. *Sustainable Energy Technologies and Assessments*, *17*, 68–76. https://doi.org/10.1016/j.seta.2016.08.004.
48. Kavya, M., & Jayalalitha, S. (2021). Developments in Perturb and observe algorithm for maximum power point tracking in photo voltaic panel: A review. *Archives of Computational Methods in Engineering, 28*(4), 2447–2457. https://doi.org/10.1007/s11831-020-09461-x
49. Khan, M., & Mathew, L. (2016). Different kinds of maximum power point tracking control method for photovoltaic systems: A review. *Archives of Computational Methods in Engineering, 24*, 855–867. https://doi.org/10.1007/s11831-016-9192-1
50. Krishnan, A., Balasubramanian, R., Kathirvelu, P., Simon, S. P., & Amirtharajan, R. (2014). Maximum power point tracking of photovoltaic generation system using artificial neural network with improved tracking factor. *Journal of Applied Sciences, 14*, 1858–1864. https://doi.org/10.3923/jas.2014.1858.1864
51. Kundur, P. S., & Malik, O. P. (2022). *Power system stability and control*. McGraw-Hill Education.
52. Naruei, I., & Keynia, F. (2021). A new optimization method based on COOT bird natural life model. *Expert Systems with Applications*, *183*, 115352. https://doi.org/10.1016/j.eswa.2021.115352.
53. Power Engineering Society. (2007). IEEE guide for the application of protective relays used for abnormal frequency load shedding and restoration. *IEEE Std C37.117-2007* (pp. 1–55). https://doi.org/10.1109/IEEESTD.2007.4299516